

## Examination of the flow near the leading edge of attached cavitation. Part 2. Incipient breakdown of two-dimensional and axisymmetric cavities

By A. TASSIN LEGER<sup>1</sup> L. P. BERNAL<sup>2</sup> AND S. L. CECCIO<sup>1</sup>

<sup>1</sup>Department of Mechanical Engineering and Applied Mechanics, University of Michigan, Ann Arbor, MI 48109-2121, USA

<sup>2</sup>Department of Aerospace Engineering, University of Michigan, Ann Arbor, MI 48109-2118, USA

(Received 27 August 1997 and in revised form 11 May 1998)

Local and global three-dimensionality of cavity interfaces near detachment was examined. Cavities forming on hydrophilic test objects at higher Reynolds numbers ( $Re > 10^5$ ) exhibited a local flow structure in the cavity interface called 'divots'. Divots resulted from a local breakdown of the two-dimensional laminar boundary separation. Divots did not form on hydrophobic test objects. Instead, at higher Reynolds numbers ( $Re > 10^5$ ), the cavity at detachment was composed of a series of wedge shaped structures. Flows with strong adverse pressure gradients upstream of cavity detachment exhibited only local three-dimensionality near one cavity detachment. Flows with weak adverse pressure gradients upstream of cavity detachment were more susceptible to breakdown into global three-dimensionality. This was the case for cavitation on the hydrofoils. Holographic particle imaging velocimetry (HPIV) was used to examine the spanwise and streamwise variation of the flow upstream of the cavity detachment. Three-dimensionality of the cavity detachment was associated with strong variations of the flow upstream of the cavity in the direction perpendicular to the mean flow direction.

---

### 1. Introduction

Nominally two-dimensional cavities which form on smooth two-dimensional hydrofoils and axisymmetric bodies will exhibit three-dimensional cavity patterns very near the region of cavity detachment in the spanwise or circumferential direction as the Reynolds number increases. Brennen (1970) examined the formation of cavity fingers as they occur on axisymmetric bluff bodies. He found that the formation of the fingers was strongly related to the flow Reynolds number and that polymer additives to the fluid also modified the formation of these structures. Changes in the liquid/vapour interfacial tension, however, did not significantly affect the formation and appearance of the cavity fingers. Analogous flow structures occur in cavity flows in bearing crevices. A review of such cavitation in bearings is provided by Dowson & Taylor (1979). Jacobson & Hamrock (1983) observed strikingly different cavitation patterns in dynamically loaded journal bearings with surface materials of either aluminium or Teflon. The overall geometry of the cavitation region did not vary with the surface material. However, the cavitating region on the aluminum surface consisted of small individual bubbles while the cavitation on the Teflon surface consists of a single

bubble with many intricate branches. Savage (1977*a,b*) examined incipient instability of the cavity interface for cavity flows in journal bearings with metal (and therefore hydrophilic) bearing surfaces. The formation of a periodic surface wave pattern was related to the liquid/vapour interfacial tension, the pressure gradients near the cavity interface, and the Taylor–Saffman number of the flow. Two-dimensional cavities on axisymmetric bodies or hydrofoils can break down into multiple partial cavities (‘streak’ or ‘spot’ cavitation). In general, it is unclear when a largely two-dimensional or axisymmetric flow body will produce three-dimensional attached cavitation. In the present work, the flow near the cavity detachment region will be examined with regard to the breakdown of a nominally two-dimensional cavity.

## 2. Experimental methods

Flow visualization techniques (dye injection, streak visualization and planar particle imaging velocimetry (PIV)) were employed for qualitative and quantitative flow analysis and are described in Tassin Leger & Ceccio (1998) (hereafter referred to as Part 1), along with a description of the blow-down water tunnel (BDWT) and the brass and Teflon test objects. Particular to this study is the use of a glass hydrofoil to examine the spanwise flows near the region of cavity detachment using holographic particle image velocimetry (HPIV).

In-line HPIV in a direction perpendicular to the water flow was used to determine the three-dimensional velocity field in the neighbourhood of the attached cavity. Pulsed laser light was used to create a double-exposed hologram of a particle-seeded flow. The movement of the particles during the known time delay between each hologram exposure gave the local velocity of the flow in three dimensions. A complete description of this technique is provided by Vikram (1992). It was necessary to examine the spanwise variation of the flow over the test object, and this was achieved by fabrication of an optically transparent hydrofoil through which a beam of collimated light could be transmitted. The hydrofoil was made of glass which was not optically matched to the surrounding liquid. Therefore the hydrofoil was designed with the embedded shape of a cylindrical lens. The lens shape permits a known distortion to the holographic recording system, which can be optically corrected for by an appropriate cylindrical lens outside the test section. The hydrofoil was mounted with two optical flats in the test section windows parallel to the hydrofoil surface such that there was optical access through the test section in the direction through the hydrofoil.

The optical setup for the HPIV in the BDWT is shown in figure 1. Two pulsed Quanta Ray GCR 130-30 Nd-YAG lasers were used to create two light pulses each with a wavelength of 532 nm. The light from the two lasers was first made collinear. The laser light passed through plano-convex lens L1 (focal length = 50 mm), pinhole P ( $d = 100 \mu\text{m}$  or less), achromatic lens L2 (focal length = 400 mm), and cylindrical lens L3 (focal length =  $-300$  mm). After L3, the light passed into the test section through an optical flat and then through the cylindrical lens-shaped transparent hydrofoil. The light, which was then collimated, passed through the region of interest, then through another optical flat, and was finally recorded on the holographic plate. While immersed in water, the effective focal length of the hydrofoil cylindrical lens was approximately 908 mm. The time between exposures was measured for each image by recording the Q-switch synchronization signals of the lasers using a Hewlett Packard 54620A 16 Channel 500 Megasamples/second Logic Analyzer. The typical pulse separation was 20  $\mu\text{s}$  with the time interval was known to within 50 ns.

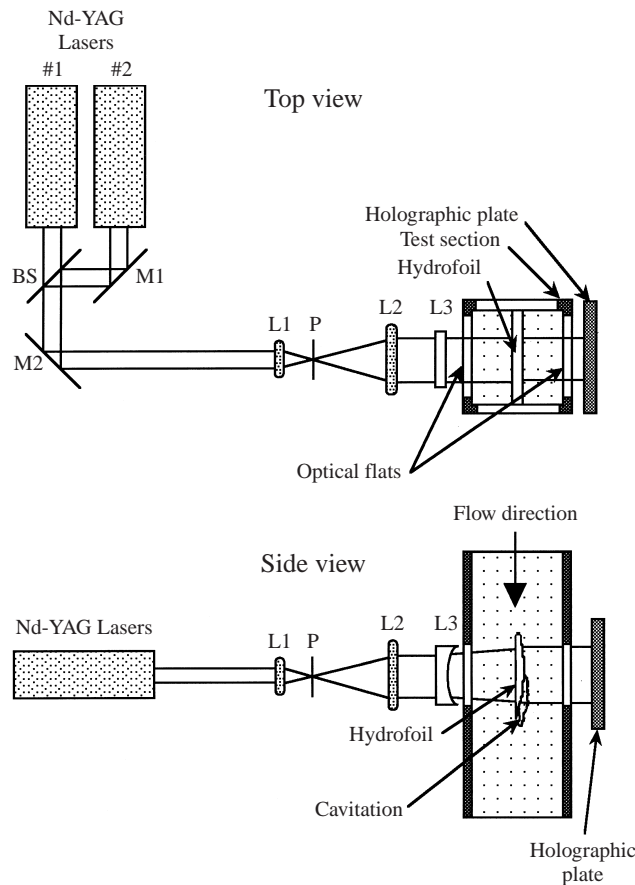


FIGURE 1. The optical setup for holographic particle image velocimetry (HPIV) in the blow-down water tunnel.

To reconstruct the image, an expanded and collimated beam of light from a Spectra Physics model 124A 30 mW He-Ne laser was directed perpendicular to the developed hologram. A microscope objective connected to a video camera was used to magnify and view the particles on the hologram. The hologram was mounted on an  $(x, y)$ -plane traversing system and the camera was mounted on a  $z$ -axis traverse. These traverses allow the microscope objective to focus at any point in the reconstructed hologram. Particle pairs were located and their positions were stored in a computer file. Knowing the particle displacement and the time between the double exposure, the velocity can be calculated. Directional discrimination was not required since the local flow was not expected to deviate significantly from the uniform free-stream flow.

The smallest particle which could be imaged with this setup was  $25\ \mu\text{m}$  in diameter. This size limit resulted from imperfections in the laser beam, optical train, and reconstruction process. Also, when the cavity was primarily straight across, the leading edge of the cavity produced diffractions which interfered with reconstruction close to the interface. The centres of the particle pairs were determined within 2 pixels, which resulted in an uncertainty of  $\pm 2\%$  in the velocity measured in the  $(x, y)$ -plane. The resolution of the  $z$ -position measurement was significantly less than that of the  $(x, y)$ -position measurement. This is characteristic of in-line holography.

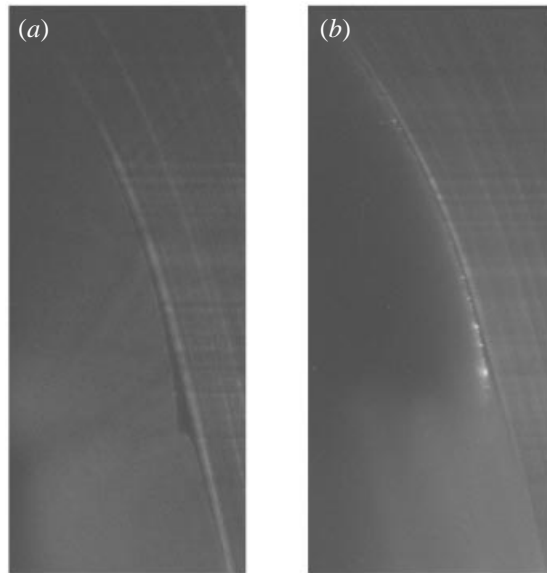


FIGURE 2. Side views of the cavity detachment region on (a) the brass sphere (visualized with dye) and (b) the Teflon sphere (visualized with particle streaks).

Therefore, the  $z$ -velocity was not measured, but the  $z$ -location was determined for each  $(x, y)$ -particle pair. The uncertainty in the  $z$ -location was typically  $\pm 0.2$  mm.

### 3. Spanwise variation of the cavity interface near the cavity detachment for nominally two-dimensional cavities

In Part 1, the geometry of the cavity near detachment was examined for two-dimensional cavities. Figure 2 summarizes the results. For the brass test objects, the cavity has a finite thickness near the point of detachment which forms a forward facing step. The contact angle at the air/water/brass interface was approximately  $30^\circ$ . For the Teflon test objects, however, the cavity interface is much flatter with a contact angle of approximately  $150^\circ$ . The liquid/vapour surface tension,  $\gamma_{lg}$  and the difference between the work of adhesion and the work of cohesion,  $\Delta W$  are parameters of the system which will influence the geometry of two-dimensional cavity detachment. Variation in these parameters will also change the spanwise geometry of the cavity interface at detachment.

#### 3.1. Cavity appearance on the brass sphere and cylinder

Figure 3(a) shows a relatively low Reynolds number ( $Re_D \approx 1 \times 10^5$ ) flow over the brass sphere with cavitation and dye injection. A smooth axisymmetric cavity separated from the sphere. Note that the green dye gathered in a recirculating region just upstream of the cavity and slowly spread out circumferentially. A similar cavity geometry is observed on the smooth brass cylinder at low Reynolds number ( $Re_D < 1 \times 10^5$ ) in figure 4(a). The presence of the recirculating region upstream of the cavity was consistent with the streak visualization images presented in Part 1.

As the Reynolds number is increased, streamwise indentations in the cavity interface formed near the line of cavity detachment. Figures 3(c) and 4(f) present photographs of higher Reynolds number flows ( $Re_D > 1 \times 10^5$ ) over the brass sphere and cylinder.

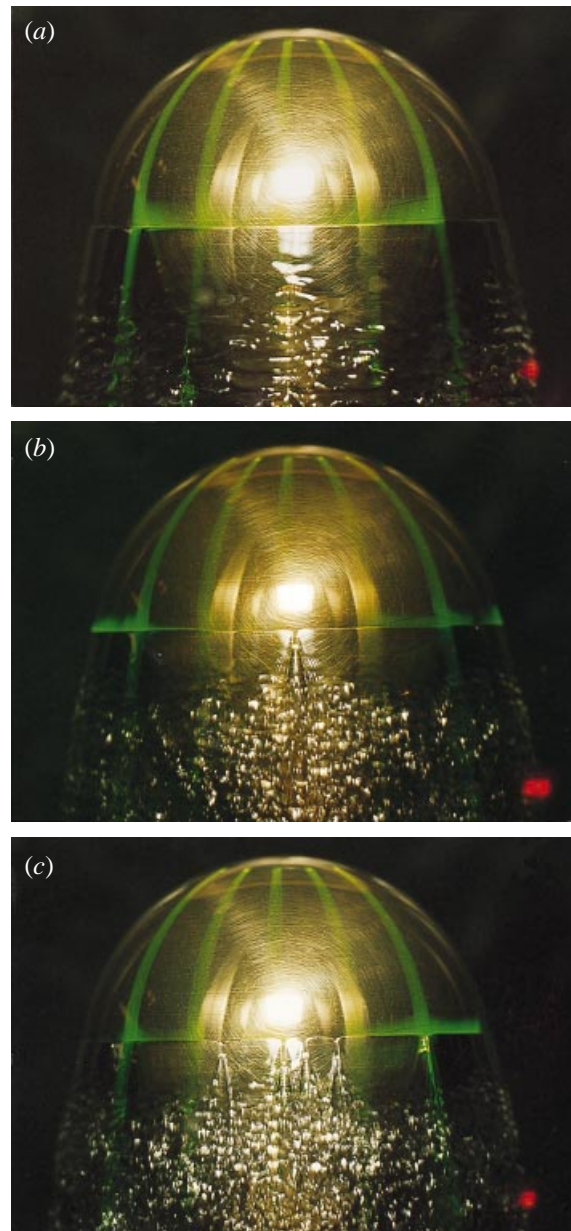


FIGURE 3. Flow near the cavity detachment on the sphere for a range of Reynolds numbers. (a) A smooth axisymmetric cavity separated from the sphere ( $Re_D = 1.2 \times 10^5$  and  $\sigma = 0.53$ ). Note that the green dye gathered in a recirculating region just upstream of the cavity and slowly spread out circumferentially. (b, c) With increasing Reynolds number, indentations in the cavity surface ('divots') form. Note that dye can flow into the indentations. (b)  $Re_D = 1.9 \times 10^5$  and  $\sigma = 0.44$  and (c)  $Re_D = 2.0 \times 10^5$  and  $\sigma = 0.47$ .

Figure 3(b) reveals that the dye can collect in the indentations in the cavity interface, suggesting that the indentations were at least partially filled with liquid. These indentations in the cavity are hereafter referred to as 'divots'. The divots could remain fixed in location, oscillate in the spanwise direction, or travel in the spanwise direction to merge with a neighbouring divot.

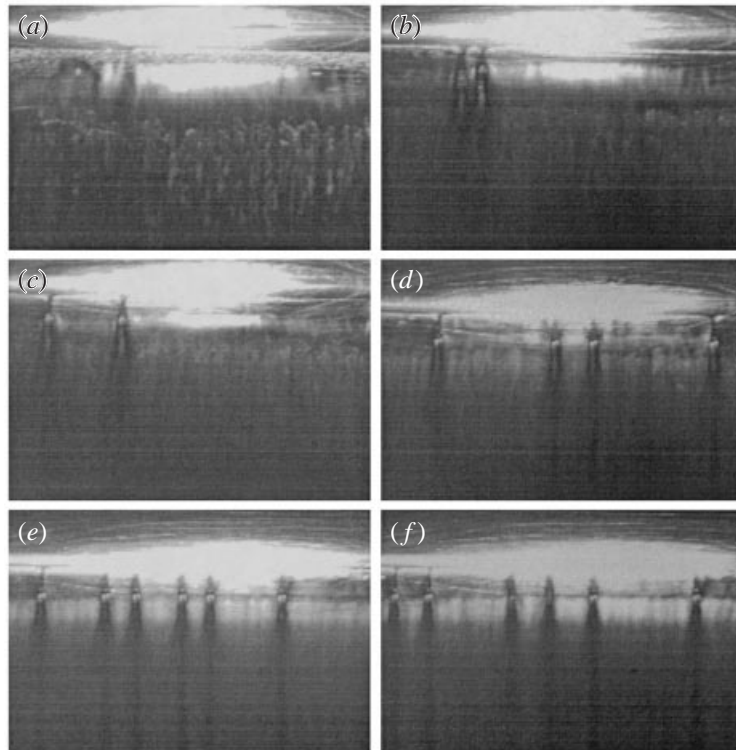


FIGURE 4. Flow near the cavity detachment on the cylinder for a range of Reynolds numbers: (a)  $Re_D = 1.2 \times 10^5$ ,  $\sigma = 1.1$ ; (b)  $Re_D = 1.5 \times 10^5$ ,  $\sigma = 1.2$ ; (c)  $Re_D = 1.8 \times 10^5$ ,  $\sigma = 1.2$ ; (d)  $Re_D = 2.1 \times 10^5$ ,  $\sigma = 1.3$ ; (e)  $Re_D = 2.5 \times 10^5$ ,  $\sigma = 1.3$ ; (f)  $Re_D = 2.6 \times 10^5$ ,  $\sigma = 1.3$ .

### 3.2. Formation, destruction, and structure of cavity 'divots'

Figure 5 shows a series of high speed video images which demonstrates the formation of a divot. The cavity near the detachment region was initially smooth. Next, a patchy disturbance appeared in the cavity surface, possibly caused by a travelling bubble (see Li & Ceccio 1996 for a discussion of the interaction of travelling bubbles with attached cavitation). The bubbles moved too quickly to be captured in the images, but bright streaks in the streamwise direction usually appeared about 3 ms before the patchy cavity surface was seen. Sometimes, however, the bright streaks were not observed to occur prior to the formation of a patchy cavity surface. In these cases, the cavity surface may have been disturbed by a local region of disturbed flow advected over the cavity. About 6 ms after the surface disturbance appeared on the cavity interface, a streamwise fluid filled divot would form, similar to frame (k) in figure 5.

An illustration of the divot geometry is shown in figure 6. The divot is a narrow streamwise indentation of the cavity, but the streamwise channel is not completely filled with liquid. While the photographs were not completely clear, it seems that there is a thin region of vapour which remains near the solid surface over some length of the divot channel. The narrow channel ends abruptly and striations in the cavity surface are oriented at an angle relative to the streamwise direction on both sides of the divot. These striations also suggested that there was a flow of liquid through the channel. The divots often oscillate in the spanwise direction while the length of the channel oscillates in the streamwise direction. If the divot moved from side-to-side,

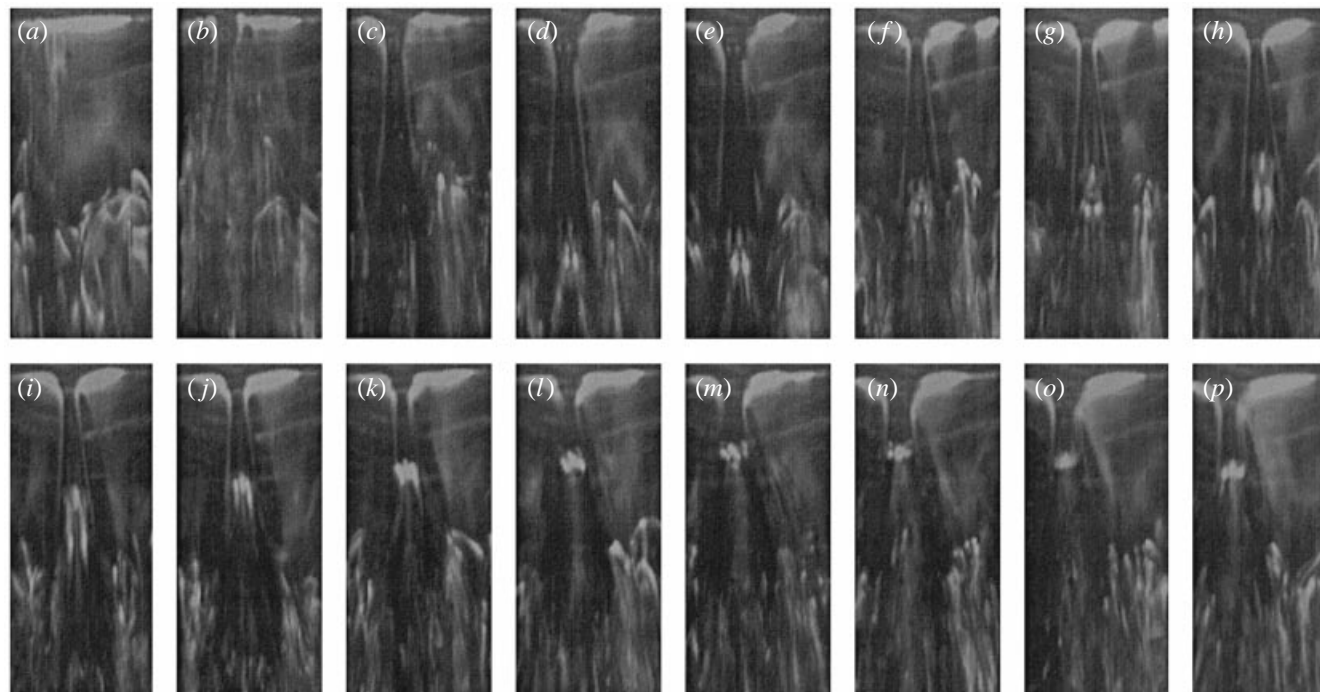


FIGURE 5. A series of video images which demonstrates the formation of a divot. The cavity near the detachment region was initially smooth. Next, a patchy disturbance appeared in the cavity surface, possibly caused by a travelling bubble. After 6 ms, a surface disturbance appears on the cavity interface leading to the formation of a 'divot'. Frames are taken in 0.5 ms increments. Frames (a-e) correspond to time 0–2.0 ms; frames (f-p) correspond to time 5.5–10.5 ms.

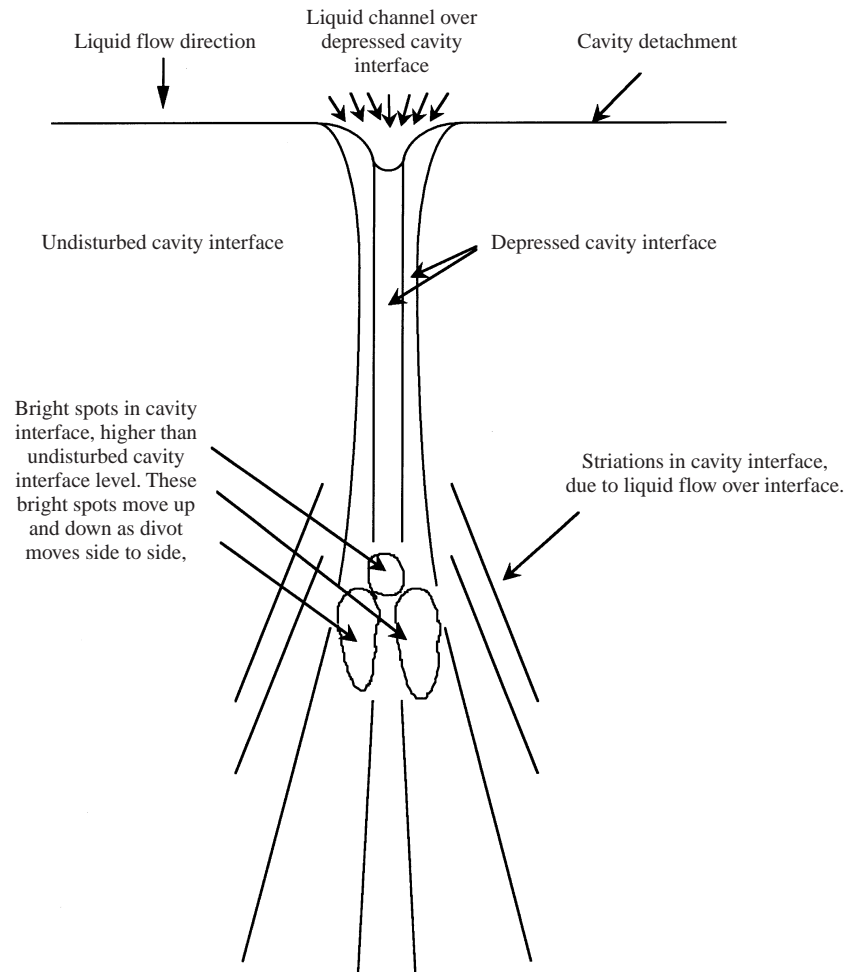


FIGURE 6. Schematic diagram of a 'divot'.

the channel length would grow and shorten. The channel length reaches its maximum when the divot is at the extreme extent of its periodic spanwise motion. If the divot is not moving, the channel length remains relatively constant. The streamwise length of the divot varies with changes in the free-stream Reynolds number and cavitation number. Figure 7 shows the measured length of the divot for varying flow conditions on the cylinder. Five measurements of the same divot at different times in the blow-down were recorded and averaged for each data point, to smooth out the effect of the divot oscillations. The length of the divot channel increased with increasing Reynolds number and increasing cavitation number.

Perturbations of the flow near the cavity separation would often cause the formation of divots. During the experiments, a re-entrant jet would periodically form at the closure of the super-cavity downstream of the test object, and the re-entrant flow would result in the production of liquid drops. These drops would often strike the cavity interface and result in divot formation. In addition, divots could be created 'on demand' by using a focused laser beam to ionize the water near the surface of the test object just upstream of the stagnation point. The growth and collapse of a

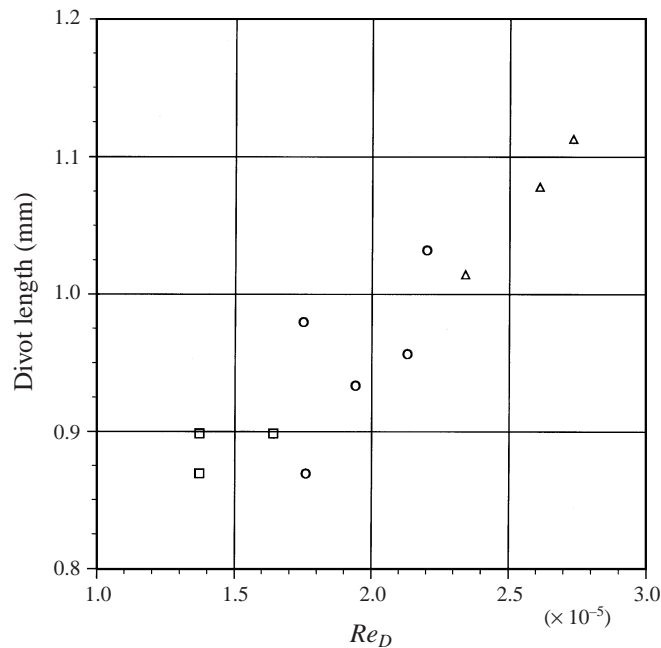


FIGURE 7. The average length of the divot for varying flow conditions on the cylinder.  
 □,  $\sigma = 1.12$ – $1.18$ ; ○,  $\sigma = 1.21$ – $1.25$ ; △,  $\sigma = 1.27$ – $1.29$ .

vapour bubble near the stagnation point would create a disturbance in the boundary layer on the surface of the test object, and the disturbance would advect downstream and result in the creation of a divot (see Tassin *et al.* 1995 for a detailed description of this method of flow perturbation). The divot would not form in exactly the same spanwise location on the sphere every time and often multiple divots would form.

As the Reynolds number of the flow was increased, the rate of divot formation and the average number of divots increased. Figure 8 presents the divot formation rate as a function of Reynolds number on the brass sphere. The data points are sorted to show the frequency of the re-entrant flow as it was observed to impact the cavity interface during each experiment. Increasing the rate of re-entrant jet impacts would increase the rate of divot formation. Figure 9 presents the divot formation rate as a function of Reynolds number on the brass sphere and cylinder for flows with minimal disturbances caused by re-entrant flow. Here, divots would be created by naturally occurring disturbances in the flow. Below a certain Reynolds number, there were no divots formed at all, suggesting that the cavity interface was stable to disturbances, that there were fewer disturbances, and/or that the disturbances which occurred were of lower intensity. If the water in the blow-down tunnel was not allowed to remain still for tens of minutes before a run, many more divots would be created during the experiment, due to the presence of more free-stream nuclei and a greater intensity of the free-stream turbulence level.

These spanwise indentations in the cavity did not result from a periodic instability of the cavity interface. Brennen (1970) examined these structures as they formed on the interface of metal (hydrophillic) spheres and cylinders in polymeric solutions. He found that a circumferential disturbance near the point of cavity attachment would grow in amplitude and frequency with increasing Reynolds number, forming a stable periodic wave-like pattern at the cavity detachment point. In the present study,

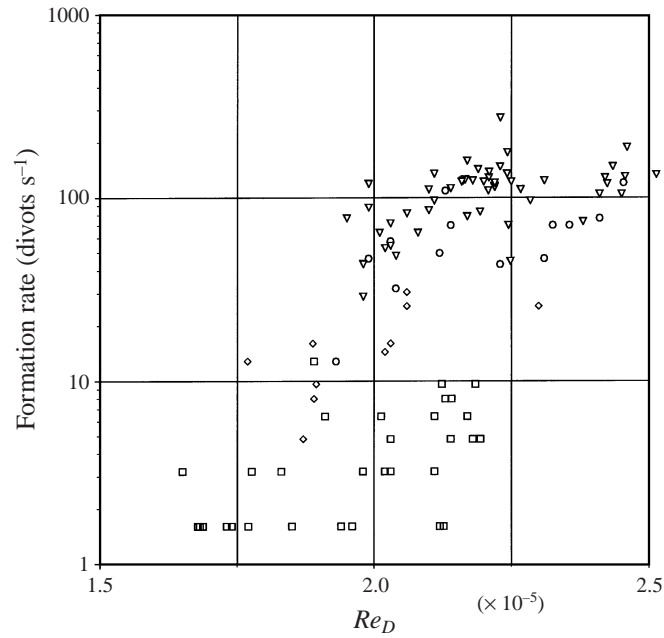


FIGURE 8. Divot formation rate as a function of Reynolds number on the brass sphere. The data are divided into four groups ranging from flows with no re-entrant jet ( $\square$ ) to those with approximately 2 ( $\diamond$ ), 6 ( $\circ$ ), and  $> 6$  ( $\nabla$ ) jet impacts per second.

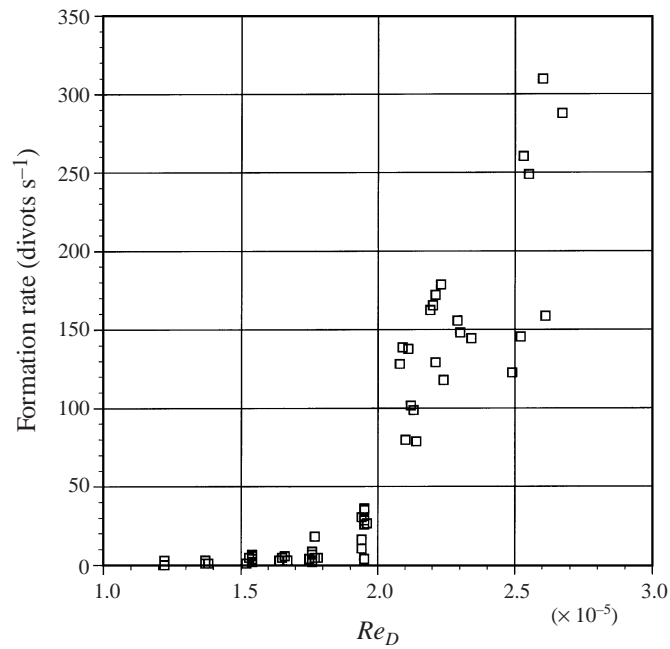


FIGURE 9. Divot formation rate as a function of Reynolds number on the brass sphere and cylinder for flows with minimal disturbance caused by re-entrant jets.

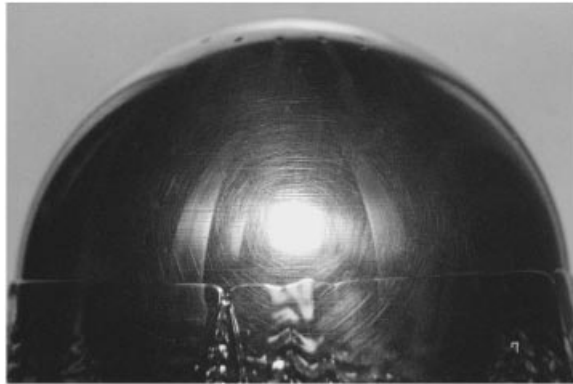


FIGURE 10. The cavity detachment region just after a divot has disappeared.

however, this mechanism of divot formation was not observed. Instead, divots were formed at random locations on the brass sphere circumference and along the length of the brass cylinder.

Destruction of a divot occurred in a process which was opposite to divot creation. A disturbance could perturb the divot and cause the divot length to decrease and the cavity to return to its undisturbed level. Figure 10 shows the cavity detachment region just after a divot has disappeared. The pointed area in the cavity detachment just to the right of the centre of the photograph is the former location of a divot. The divot disappeared when the channel of liquid was reduced in length and the interface of the cavity extended upstream of the stable streamwise position of cavity detachment. The cavity interface would oscillate and relax back into a locally two-dimensional detachment line.

These detailed observations of divot creation, persistence, and destruction indicate that the divot represents an alternative stable flow configuration at the cavity interface. The location of the cavity interface is linked to the position of laminar boundary layer separation upstream of the cavity. A local depression of the cavity interface may delay or eliminate laminar boundary layer separation in a region near the disturbance. This, in turn, leads to the formation of a local jet of liquid. Dye streak visualization suggests that the source of the jet liquid is the flow outside the boundary layer and not the recirculating flow just upstream of the cavity. Dye present in the recirculating region upstream of the cavity did not readily flow into nearby divots. However, dye streaks injected upstream of a divot could be captured by the divot, resulting in a spanwise shift of the dye stream. Thus, the flow within the divot channel has considerable streamwise momentum, and this flow is diverted up and out of the channel at the abrupt end of the divot. As such, a balance existed between the stagnation pressure of the channel flow and the local cavity pressure. This description is consistent with the data of figure 7, which shows an increase in divot length with increasing free-stream velocity. The pressure difference across the cavity resulting from liquid/vapour interfacial tension was small when compared with the ventilated cavity pressure (an interfacial curvature radius of  $100\ \mu\text{m}$  leads to a pressure difference of less than  $1\ \text{kPa}$ ), but it may be comparable to the cavity pressure of a natural vapour cavity.

Figure 11 presents two images which lend evidence to this qualitative description. Two magnified images of divots are shown for cavity flows over the brass cylinder. The flow conditions in both cases were similar, but the rate of dye injection differed. In figure 11(a), the dye was sucked into the flow because of the reduced local static

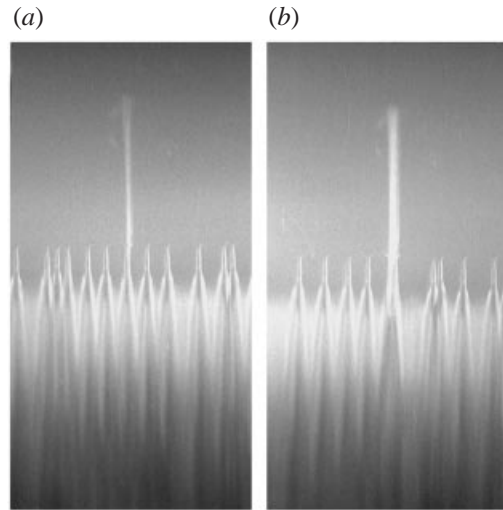


FIGURE 11. Two magnified images of divots are shown for cavity flows over the brass cylinder. (a) The dye was sucked into the flow producing a thin dye streak ( $Re_D = 9.7 \times 10^4$ ,  $\sigma = 0.8$ ). (b) A syringe was used to force dye through the hole creating a thicker jet of dye ( $Re_D = 1.7 \times 10^5$ ,  $\sigma = 1.1$ ). When the dye was sucked into the flow, the divot shown was similar to others nearby. However, when the dye was forced out of the hole on the cylinder surface, the divot was wider in comparison to other divots present. Thus, the minimal addition of streamwise momentum during dye injection widened the divot channel.

pressure at the injection hole. A thin dye streak was produced. In figure 11(b), a syringe was used to force dye through the hole, creating a thicker jet of dye. In each case, the dye stream passed directly through a divot channel. When the dye was sucked into the flow, the divot shown was similar to others nearby. However, when the dye was forced out of the hole on the cylinder surface, the divot was wider in comparison to other divots present. Thus, the minimal addition of streamwise momentum during dye injection widened the divot channel.

### 3.3. Cavity appearance on the Teflon cylinder and sphere

As shown in figure 2, the cavity on the Teflon body nearly fills the recirculation zone upstream of the cavity detachment in contrast to the brass test objects. The spanwise variation in the leading edge of these cavities was also quite different from that of the brass test objects. Figures 12 and 13 show photographs of cavitating flows on the Teflon sphere and Teflon cylinder as a function of Reynolds number. These images contrast with cavities on the brass test objects at similar test conditions as in figures 3 and 4. The detachment of the cavity did not occur along a spanwise line, even at lower Reynolds numbers. At higher Reynolds numbers, the cavity interface formed relatively large triangular-tipped points which protruded upstream of the average location of cavity detachment and remained relatively fixed in location. The triangular peaks in the cavity interface were not regularly spaced in the spanwise direction (although the variation was less on the sphere when compared with the cylinder). Individual divots were not observed at the interface of the cavity under any conditions. The triangular-tipped cavities can be considered ‘spot cavities’ which have been identified with cavitation near local surface roughness. The average surface roughness of the Teflon test objects was approximately  $1 \mu\text{m}$ , compared to a value of less than  $0.1 \mu\text{m}$  for the brass test objects. The location of the triangular cavity peaks would vary

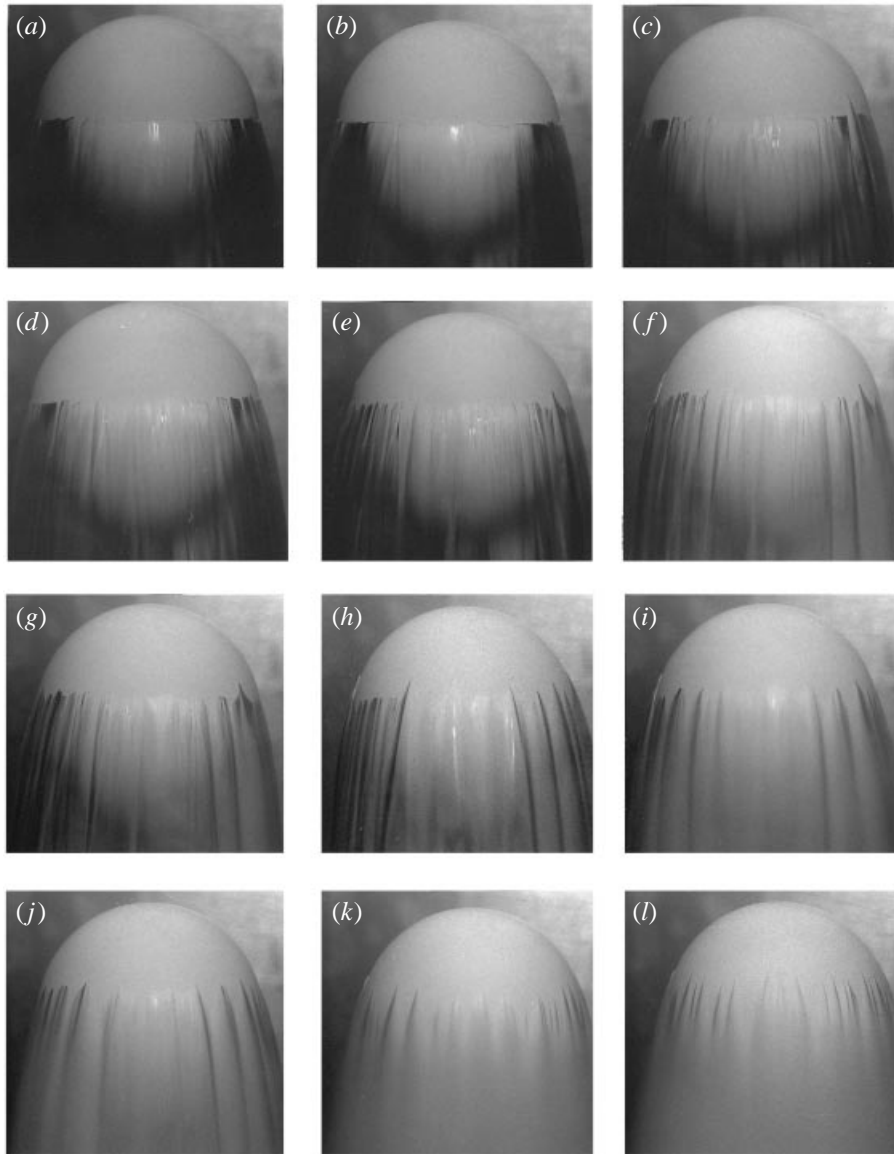


FIGURE 12. Photographs of cavitating flows on the Teflon sphere: (a)  $Re_D = 1.2 \times 10^5$ ,  $\sigma = 0.41$ ; (b)  $Re_D = 1.4 \times 10^5$ ,  $\sigma = 0.42$ ; (c)  $Re_D = 1.7 \times 10^5$ ,  $\sigma = 0.43$ ; (d)  $Re_D = 1.9 \times 10^5$ ,  $\sigma = 0.44$ ; (e)  $Re_D = 2.1 \times 10^5$ ,  $\sigma = 0.45$ ; (f)  $Re_D = 2.4 \times 10^5$ ,  $\sigma = 0.46$ ; (g)  $Re_D = 2.5 \times 10^5$ ,  $\sigma = 0.46$ ; (h)  $Re_D = 2.8 \times 10^5$ ,  $\sigma = 0.47$ ; (i)  $Re_D = 3.1 \times 10^5$ ,  $\sigma = 0.48$ ; (j)  $Re_D = 3.2 \times 10^5$ ,  $\sigma = 0.47$ ; (k)  $Re_D = 3.4 \times 10^5$ ,  $\sigma = 0.52$ ; (l)  $Re_D = 3.7 \times 10^5$ ,  $\sigma = 0.54$ .

during a test and vary from test to test. However, the peaks did consistently form at some specific locations (this can be seen in figure 12). It was concluded that only a few of the peaks were primarily caused by roughness elements. Moreover, the cavity which formed on a roughened brass sphere (with surface roughness  $5 \mu\text{m}$ ) was examined. It was found that spot cavities did not form on the roughened sphere and that the cavity detachment geometry was similar to that of the smooth sphere.

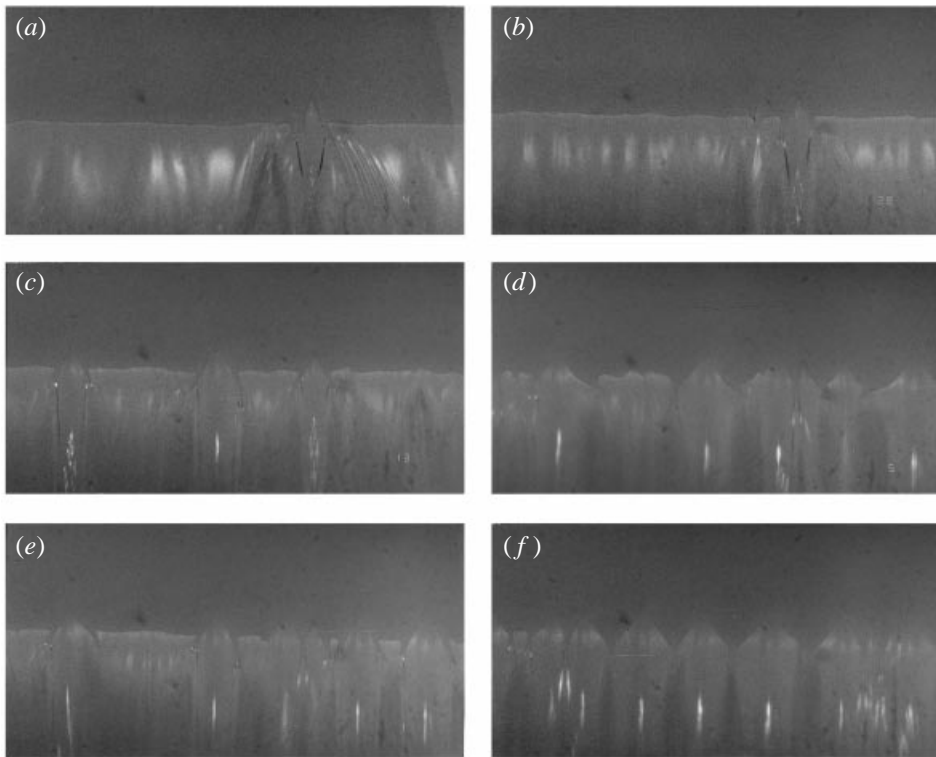


FIGURE 13. Photographs of cavitating flows on the Teflon cylinder: (a)  $Re_D = 6.9 \times 10^4$ ,  $\sigma = 0.93$ ; (b)  $Re_D = 1.0 \times 10^5$ ,  $\sigma = 1.0$ ; (c)  $Re_D = 1.2 \times 10^5$ ,  $\sigma = 1.1$ ; (d)  $Re_D = 1.4 \times 10^5$ ,  $\sigma = 1.2$ ; (e)  $Re_D = 1.7 \times 10^5$ ,  $\sigma = 1.2$ ; (f)  $Re_D = 2.0 \times 10^5$ ,  $\sigma = 1.2$ .

However, the position of the cavity tips would vary during the course of the experiment, unlike spot cavities which form as the result of relatively large surface roughness elements. The variations in the cavity geometry at the point of cavity detachment resulted in streamwise striations in the cavity interface (figure 14*b*). This can be contrasted with the cavity which formed on the brass test object (figure 14*a*). Thus, local changes in the geometry of the cavity detachment produced global changes on the cavity surface.

#### 4. Breakdown of the two-dimensional cavity detachment

The divots on the hydrophilic brass test objects and wedge-shaped structures on the hydrophobic Teflon test objects reveal a local breakdown of the two-dimensional flow near the cavity detachment. However, cavities on the hydrofoils (which were hydrophilic) exhibited a variety of patterns. The cavity could be largely two-dimensional, with the cavity detachment forming in a spanwise line perpendicular to the flow. Divots were observed near the region of cavity detachment. The cavity detachment line could be distorted but continuous in the spanwise direction. Or, the cavity would break down into individual attached patches of cavitation which were separated by wide regions of fluid (much wider than the divot width). Examples of these three cases for flows over the NACA 63<sub>1</sub>A012 hydrofoil are shown in figure 15.

HPIV was used to examine the streamwise and spanwise flows near the region of three-dimensional cavity detachment. A hologram of the seeded flow was acquired

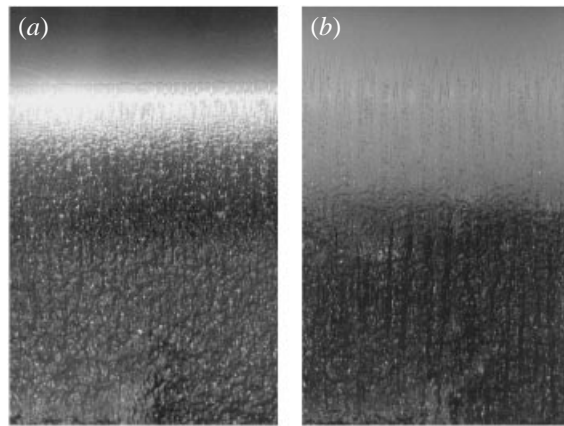


FIGURE 14. Appearance of the cavity downstream of the point of cavity detachment for (a) the brass cylinder and (b) the Teflon cylinder ( $Re_D = 1.2 \times 10^5$ ,  $\sigma = 1.2$ ).

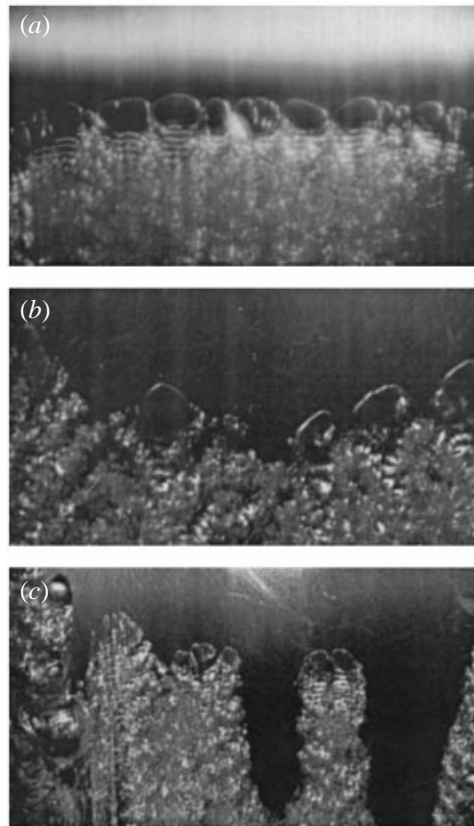


FIGURE 15. Three cavities as they formed on the NACA 63<sub>1</sub>A012 hydrofoil: (a) the cavity is largely two-dimensional, with divots at the cavity interface and the cavity detachment forming in a spanwise line perpendicular to the flow, (b) the cavity detachment line is distorted but continuous, or (c) the cavity would break down into individual patches of cavitation which were separated by wide regions of fluid (much wider than the divot width) ( $Re_C = 1.1 \times 10^6$ ,  $\sigma = 0.4$ ).

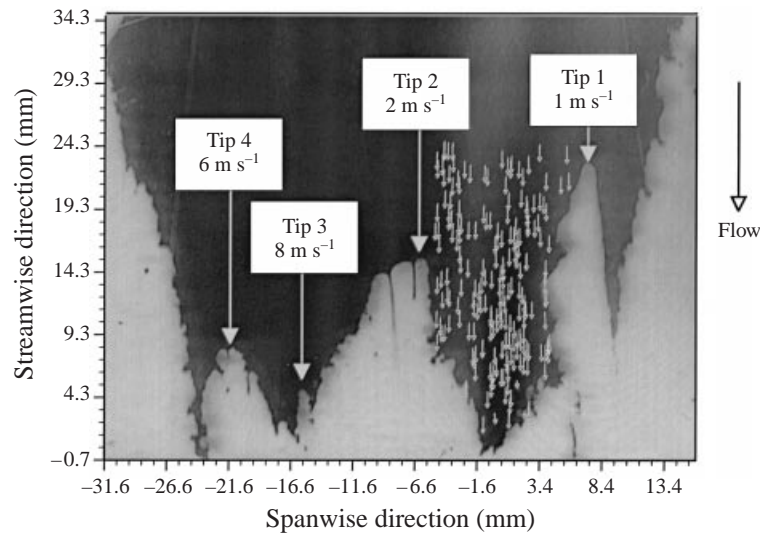


FIGURE 16. Reproduction of the unreconstructed holographic film plate taken of the cavitating flow over the custom glass hydrofoil. The outline of the cavity is visible. Also shown are velocity vectors in the interrogation region determined by HPIV. The position of these vectors is at varying distances from the surface of the hydrofoil.

through the custom designed glass hydrofoil. The flow near the cavity detachment was examined and local velocity vectors were measured in a volume of fluid near the hydrofoil surface. Figure 16 shows an image of the unreconstructed holographic film plate, and the outline of the cavity is visible. Also shown are velocity vectors in the interrogation region. The position of these vectors is at varying distances from the surface of the glass hydrofoil.

The cavity flow shown in figure 16 is largely three-dimensional. Unlike the cavity detachment on the sphere and cylinder, the point of cavity detachment is not static. Instead, the cavity interface was observed to be moving with a velocity of between 0.1 and 1 times the local fluid velocity near the point of cavity detachment. Four portions of the cavity are identified in figure 16 as ‘tips’ 1 to 4. Tip 2 is approximately at the position of two-dimensional cavity separation. Also, the geometry of tips 1 and 2 locally resemble that of the two-dimensional cavity detachment. These interfaces move the least. Tips 3 and 4, however, are located in regions downstream of the original point of two-dimensional cavity separation. The interface there moves with a velocity which is on the order of the free-stream velocity, revealing a highly dynamic cavity. It is unclear whether the cavity interface is translating on the foil surface or oscillating around a fixed cavity location.

Figure 17 shows three images of unreconstructed holograms taken of three cavity flows. A shaded box represents the region of interrogation where velocity vectors were measured after holographic reconstruction. Figure 17(c) is a portion of the cavity shown in figure 16. The velocity vectors from these three images are plotted in figures 18, 19, and 20. For each of these conditions,  $\alpha = 3.0^\circ$ , and  $\sigma \approx 0.4$ . Figure 18 presents the velocity vectors measured from the hologram in figure 17(a). This cavity is largely two-dimensional. Six plots present the data for vectors recorded up to 20 mm above the hydrofoil surface. Data are plotted with respect to both the streamwise and spanwise directions and are sorted into groups representing varying distances

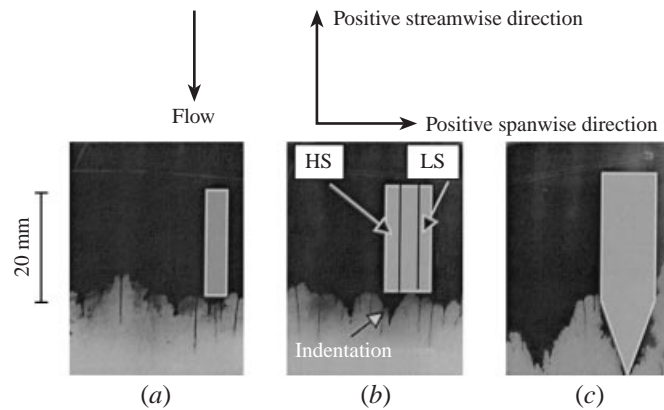


FIGURE 17. Three images of unreconstructed holograms showing an outline of a cavity on the custom hydrofoil. The HPIV interrogation region is the lighter-shaded box. In (b), the interrogation region is divided into three parts where 'HS' and 'LS' are regions of relatively higher and lower flow velocity. For the three cases,  $Re_c \approx 1 \times 10^6$ ,  $\sigma \approx 0.4$ , and  $\alpha = 3.0^\circ$ .

above the hydrofoil surface. The spanwise velocities are on the order of 2% of the streamwise velocity, and there is no correlation of either the streamwise or spanwise velocity with variations in the spanwise cavity geometry. A mild adverse pressure gradient is observed upstream of the cavity separation (figure 18e).

Figure 19 presents the velocity vectors measured from the hologram in figure 17(b). Data are sorted into groups representing varying distances above the hydrofoil. The flow near a significant indentation in the cavity is examined. Unlike the flow near the largely two-dimensional cavity, the flow near the cavity separation varies significantly in the spanwise direction (figures 19c and 19d). The spanwise velocity is still small, but the streamwise velocity decreases by nearly 10% from across the spanwise extent of the interrogation region. The cavity indentation corresponds to the region of higher streamwise velocity. In the spanwise region between 2 and 4 mm (the region of highest shear), the streamwise velocity decreases as the surface of the hydrofoil is approached. Also, a weak correlation between the spanwise velocity and the distance above the hydrofoil can be found in this spanwise segment. In general, the vectors closest to the hydrofoil have a positive component of spanwise velocity, and the velocity vectors farther from the foil surface have a negative spanwise velocity. This suggests a local vortex with components in both the spanwise and streamwise directions. Upstream of the cavity, a mild adverse pressure gradient is found in the streamwise direction (figure 19e) although the magnitude of the gradient varies in the spanwise direction.

Figure 20 presents the velocity vectors measured from the hologram in figure 17(c) where the two-dimensionality of the cavity has broken down. The spanwise velocity components are correlated with the cavity geometry; vectors with positive spanwise velocities are located on the left side of the interrogation region, and those with negative spanwise velocities are on the right side (figure 20d). There is little variation of the streamwise velocity in the spanwise direction. Again, a mild adverse pressure gradient exists upstream of the cavity detachment (figure 20e). The location of the decelerating flow is now further downstream, as is the point of cavity separation.

The decelerating flows upstream of the cavity separation are compared in figure 21. Data are plotted for the flows in figures 17(a), 17(c), and two sets data are presented for the flow in 17(b) representing the two extents of the flow in the spanwise direction

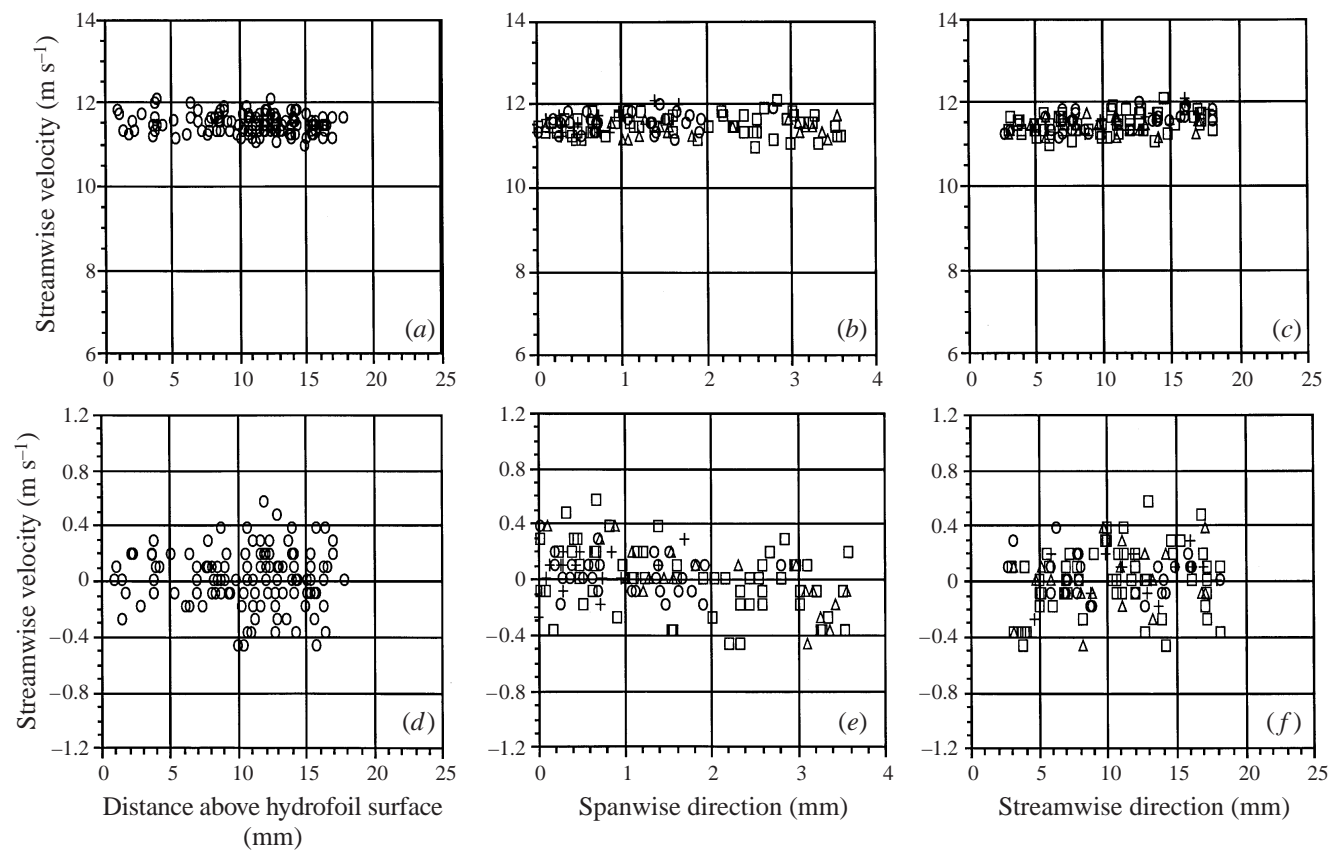


FIGURE 18. The velocity vectors measured from the interrogation shown in figure 17(a). Six plots present the data for vectors recorded up to 20 mm above the hydrofoil surface. Data are plotted with respect to both the streamwise and spanwise directions, and are sorted into groups representing varying distances above the hydrofoil surface:  $< 5$  mm (+), 5 to 10 mm (O), 10 to 15 mm ( $\square$ ),  $> 15$  mm ( $\triangle$ ).

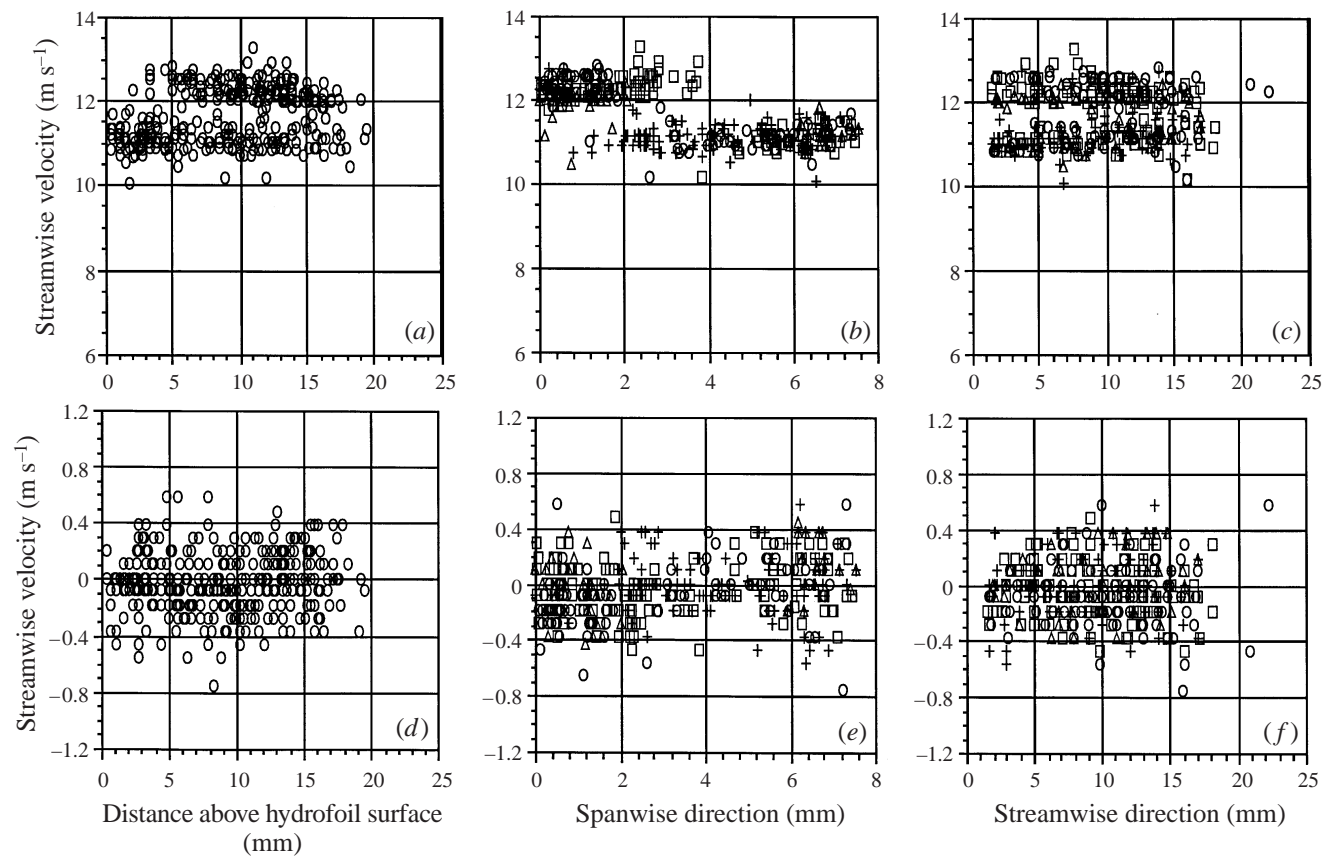


FIGURE 19. As figure 18 but from the interrogation shown in figure 17(b).

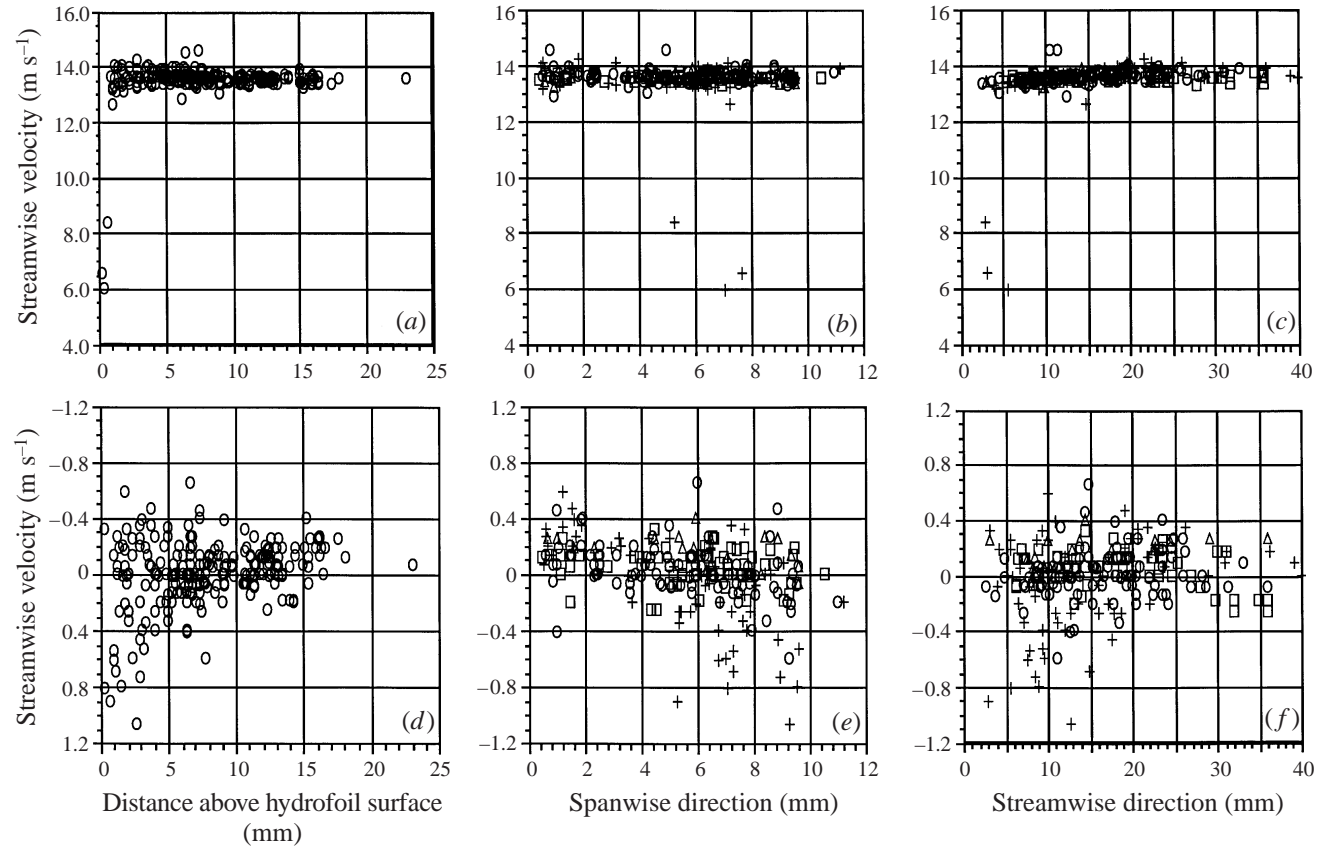


FIGURE 20. As figure 18 but from the interrogation shown in figure 17(c).

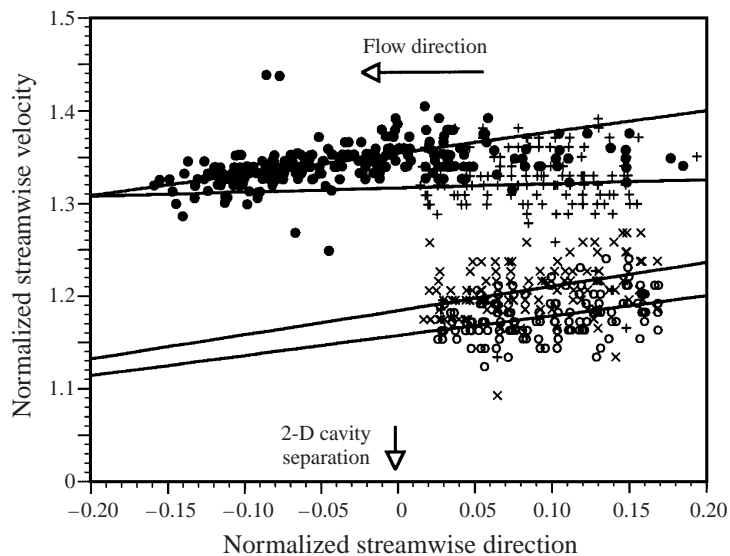


FIGURE 21. The streamwise velocity plotted against the streamwise direction for the regions defined in figure 17. The streamwise velocity is normalized with the free-stream velocity, and the streamwise direction is normalized with the chord length: figure 17(a) ( $\bullet$ ), figure 17(b), HS (+), figure 17(b) LS ( $\times$ ), and figure 17(c) ( $\circ$ ). Lines are fit through the data, and for the data of 17(a), only that portion of the data downstream of the point of two-dimensional cavity detachment is correlated to the line.

(labelled 'HS' and 'LS' for the regions of high- and low-speed streamwise velocity). The streamwise velocity is normalized with the free-stream velocity, and the streamwise position is normalized with the chord length. The magnitude of the streamwise velocity is greater for cases where the cavity detachment is further downstream when compared with the position of two-dimensional separation. The magnitude of flow deceleration upstream of the cavities is approximately equal, except for the flow upstream of the cavity indentation shown in figure 17(b). In this case, the deceleration is weaker.

It was shown in Part 1 that the presence of a cavity significantly modifies the overall pressure field, ultimately leading to a change in the boundary layer separation upstream of the cavity. The location of flow separation can be moved downstream with a weakening of the adverse pressure gradient near cavity detachment. The data presented above indicate that a weak adverse pressure gradient exists upstream of three-dimensional cavity detachment. If a strong adverse pressure gradient existed upstream of the cavity detachment, the flow near detachment would be less susceptible to local flow variations and the cavity detachment would remain relatively two-dimensional. This was the case for the sphere and cylinder. However, if a weak adverse pressure gradient existed upstream of the cavity detachment, the flow near detachment would be much more susceptible to local perturbations. Ultimately, any large variation in the cavity geometry will lead to further variation of the flow field upstream of detachment leading to the breakdown of the two-dimensional cavity detachment. This was evident on the hydrofoil cavity flows. It is important to note that local turbulent transition in the boundary layer upstream of cavity detachment can lead to local reattachment of the boundary layer and destruction of the cavity, as shown by Li & Ceccio (1996). This phenomenon will also lead to the breakdown of a two-dimensional cavity detachment line.

## 5. Conclusion

Cavities forming on the hydrophilic test objects exhibited a local three-dimensional flow structure near the cavity interface. These ‘divots’ appeared at moderately high Reynolds numbers, and were caused by local disturbances of the cavity interface. Divots resulted from a local breakdown of the two-dimensional laminar boundary separation upstream of the cavity detachment. The divot formed when a small jet of fluid penetrated into the cavity. Divots did not form on the hydrophobic (Teflon) test objects. Instead, the cavity detachment region was composed of wedge-shaped features. These features changed the appearance of the cavity interface compared to cavities on the hydrophilic test bodies. These local flow structures can lead to significant changes in the cavity interface downstream of the cavity detachment.

Brennen (1970) examined the detachment region of ventilated cavitation on spheres. For flows in pure water, no divots were observed up to  $Re_D \times 10^4$ , which was also the case in this study. If polymers were added to water, a periodic distortion of the cavity detachment line was observed. The wavelength of the disturbance decreased with increasing free-stream velocity until divot-like structures were observed. This mechanism was not observed in the present study for the formation of divots in clean water. Moreover, Savage (1977*a,b*) describes fingering which occurs on cavities formed in bearings. Savage related the formation of divot-like structures to an instability at the cavity interface. He related the stability of the flow to the Taylor–Saffman number and the pressure gradient upstream of the cavity. Savage showed that the cavity fingers originated from a periodic disturbance of the cavity interface for a range of Taylor–Saffman numbers  $0.1 < \mu U_o / \lambda_{lg} < 3$ . In the present study, the Taylor–Saffman number varied between  $0.03 < \mu U_o / \lambda_{lg} < 0.3$ . A periodic instability was not observed on the cavity interfaces in this study. While the structures that Brennen and Savage observed are analogous to the divots in the present study, the mechanisms which create them are quite different. The structures observed by Brennen may be precursors to divots which form at higher Reynolds number, and the periodicity of the cavity disturbance probably resulted from the presence of the long chain polymers in the recirculating region upstream of the cavity detachment. Savage examined lubrication flows where the relationship between liquid pressure, viscosity, and interfacial tension will differ significantly from the flows under consideration here.

A flow which has a strong adverse pressure gradient upstream of the cavity will be less likely to exhibit strong three-dimensionality at the cavity detachment. This was the case for flows over the sphere and cylinder. However, a flow with a weak adverse pressure gradient upstream of the cavity will be susceptible to three-dimensional breakdown of a nominally two-dimensional cavity. This was the case for the hydrofoils. The flow near the hydrofoil surfaces could vary significantly in the spanwise direction with corresponding variation in the cavity geometry. In these cases, two-dimensional models of cavity detachment are not adequate to describe the process of three-dimensional cavity detachment. Such modelling is adequate if there is a strong adverse pressure gradient upstream of the cavity detachment.

The authors would like to acknowledge the substantial assistance of Daniel Wasserman, Noah Shirk, Travis Roth, and Kathy Laberteaux for their assistance in the reduction of the data. This work was supported by the Office of Naval Research contract numbers N00014-93-1-0029 and N00014-96-1-0076 with Dr Edwin P. Rood as the contract monitor.

REFERENCES

- BRENNEN, C. 1970 Some cavitation experiments with dilute polymer solutions. *J. Fluid Mech.* **44**, 51–63.
- DAVIES, J. T. & RIDEAL, E. K. 1961 *Interfacial Phenomena*. Academic Press.
- DOWSON, D. & TAYLOR, C. M. 1979 Cavitation in bearings. *Ann. Rev. Fluid Mech.* **11**, 35–66.
- JACOBSON, B. O. & HAMROCK, B. J. 1983 High-speed motion picture camera experiments of cavitation in dynamically loaded journal bearings. *J. Lubrication Technol.* **105**, 446–452.
- LI, C.-Y. & CECCIO, S. L. 1996 Interaction of single travelling bubbles with the boundary layer and attached cavitation. *J. Fluid Mech.* **332**, 329–353.
- SAVAGE, M. D. 1977*a* Cavitation in lubrication. Part 1. On boundary conditions and cavity-fluid interfaces. *J. Fluid Mech.* **80**, 743–755.
- SAVAGE, M. D. 1977*b* Cavitation in lubrication. Part 2. Analysis of wavy interfaces. *J. Fluid Mech.* **80**, 757–767.
- TASSIN, A. L., LI, C.-Y., CECCIO, S. L. & BERNAL, L. P. 1995 Velocity field measurements of cavitating flows. *Exps. Fluids* **20**, 125–130.
- TASSIN LEGER, A. & CECCIO, S. L. 1998 Examination of the flow near the leading edge of attached cavitation. Part 1. Detachment of two-dimensional and axisymmetric cavities. *J. Fluid Mech.* **376**, 61–90.
- VIKRAM, C. S. 1992 *Particle Field Holography*. Cambridge University Press.